Science and Technology Indonesia
e-ISSN:2580-4391 *p*-ISSN:2580-4405
Vol. 10, No. 3, July 2025

Research Paper

Construction of Ternary Heterojunction g-C_3N_4/$BiVO_4$/GQDs Nanocomposite and Its Methylene Blue Photodegradation Performance

Heroldinho Arieveali[1], Tien Setyaningtyas[1], Kapti Riyani[1], Anung Riapanitra[1*]

[1]*Department of Chemistry, Faculty of Mathematics and Natural Sciences, Jenderal Soedirman University, Central Java, Purwokerto, 53122, Indonesia*
***Corresponding author**: anung.riapanitra@unsoed.ac.id

Abstract
Ternary heterojunction g-C_3N_4/$BiVO_4$/GQDs (CBG) composite photocatalysts were successfully made by high-temperature solid-state method. The prepared CBG photocatalyst was used to degrade the methylene blue (MB) solution under the simulation of visible light irradiation. The analysis of photocatalytic activity was carried out in the parameters of mass variation of composite components, pH of MB solution, and kinetic rate measurement. The results showed that the adsorption-photocatalysis synergy effect occurred at its best in CBG-20 samples with pH 9 in MB solution with a degradation kinetic rate following the pseudo-first order within 150 min of removal time as the optimum condition that could degrade MB by 94.81%. The result showed that the photocatalytic activity of the ternary composite was higher than that of pristine g-C_3N_4, $BiVO_4$, or the binary composite of g-C_3N_4/$BiVO_4$. Trapping experiments results support the direct dual Z-scheme which shows that $\cdot O_2^-$ is the most significant radical for the photocatalytic degradation of MB. The prepared ternary composites show outstanding application prospects in wastewater treatment.

Keywords
$BiVO_4$, Ternary Photocatalyst, Direct Dual Z-scheme, Visible Light Irradiation, Methylene Blue Photodegradation

Received: 20 January 2025, Accepted: 21 April 2025
https://doi.org/10.26554/sti.2025.10.3.777-788

1. INTRODUCTION

Currently, environmental pollution, especially liquid waste, is one of the major issues that create concern. As much as 50,000 tons of textile waste is estimated to be disposed of annually with 10-30% of the unbound dye mixture from the dyeing and printing process (Dihom et al., 2022). With the increase in environmental pollution, semiconductor-based heterogeneous photocatalysis has attracted the world's attention due to its application in environmental remediation (Riapanitra et al., 2022). There are three steps of photocatalytic reactions with the use of light as a driving force, namely the generation of a charge when exposed to light followed by the separation of the charge from the mass to surfacing the catalyst. The step ends with the consumption of the charge in the surface redox reaction. Efficiency improvements can be based on being easily applied to these three steps.

$BiVO_4$ is an n-type semiconductor, has garnered considerable attention as a promising waste degradation photocatalyst owing to its non-toxic characteristics, narrow band gap of 2.4, and higher utilization of sunlight (Mansha et al., 2023). However, the photocatalytic performance of pure $BiVO_4$ requires enhancement, as its narrow band gap leads to recombination of the photo-generated charge carriers, which reduces its overall photocatalytic efficiency. The synthesis of $BiVO_4$ heterojunction composites with other carbon-based materials, such as g-C_3N_4 can be synthesized to overcome the shortcomings of $BiVO_4$. Compared to conventional heterojunctions, direct Z-scheme heterojunctions offer a highly promising approach, as they enhance the separation of photo-excited charge carriers and preserve e^- and h^+ in a potent redox capability. The material g-C_3N_4 has excellent physicochemical properties, such as good chemical stability, rapid separation as a carrier of photo-generative charges, and attractive electronic structure (Riapanitra et al., 2024). However, most heterostructure photocatalysts that have been specialized in binary heterojunctions including $BiVO_4$/g-C_3N_4 have limitations in the visible light response region and low redox capabilities in binary systems that can be a stumbling block in the application of such photocatalysts (Su et al., 2021). Li et al. (2023) successfully degraded Rhodamine B by 90.4% using Z-scheme g-C_3N_4/$BiVO_4$ photocatalyst, but in a relatively long time (5 hours).

The use of a ternary direct dual z-scheme heterojunction with GQDs can overcome those problems. Graphene Quantum Dots (GQDs) materials show promising potential to corroborate this because GQDs have excellent photostability and high specific surface area. GQDs exhibit tunable band gaps

ranging from 0 to 6 eV. These properties make GQDs highly suitable for integration with other photocatalysts in the construction of heterojunction systems such as $CuWO_4$/GQDs. Based on these merits, GQDs is frequently utilized to compound with other catalysts to construct heterojunctions such as $CuWO_4$/GQDs (Sarwar et al., 2023), GQDs/BiOBr (Liu et al., 2024), GQDs/g-C_3N_4/ZIF-67 (Zhao et al., 2024). GQDs have the potential to increase the photocatalytic activity of $BiVO_4$/g−C_3N_4 by forming a more redox capabilities and extending visible light absorption range (Cheng et al., 2022).

Combining two semiconductors together follow what it called a Z-scheme heterojunction. The operational framework of Z-scheme heterojunction is categorized into single (binary) and dual (ternary) framework. Compared to binary Z-scheme photocatalysts, dual ternary Z-scheme heterojunction exhibits higher charge separation, eminent redox capacity, and high charge carrier concentration (Kumar et al., 2022; Yu et al., 2022.

In this study, g-C_3N_4, $BiVO_4$, and GQDs were developed to create a heterojunction direct dual Z-scheme composite of g-C_3N_4/$BiVO_4$/GQDs which has not been previously accounted in other report and was implemented to enhance the removal of MB in aqueous solutions. Nanosheets g-C_3N_4, nano-sized $BiVO_4$, and GQDs with particle sizes of 6-10 nm were prepared in advance by ordinary calcination, coprecipitation, and hydrothermal methods respectively which were then mixed to synthesize g-C_3N_4/$BiVO_4$/GQDs composites.

2. EXPERIMENTAL SECTION

2.1 Materials

The materials used include bismuth (III) nitrate pentahydrate ($Bi(NO_3)_3.5H_2O$), ammonium metavanadate (NH_4VO_3), nitric acid (HNO_3), sodium hydroxide (NaOH), sodium nitrate (NaNO3), hydrochloric acid (HCl), methylene blue, ethanol, methanol, isopropyl alcohol, ammonium oxalate, benzoquinone, graphite powder, and melamine. No purification step was performed. All chemicals were high purity manufactured by Merck.

2.2 Methods

2.2.1 Synthesis of $BiVO_4$

The BiVO4 photocatalyst was prepared using a modified coprecipitation method of El-Yazeed et al. (2021). A precursor of 1 millimole of $Bi(NO_3)_3.5H_2O$ in 8 mL of 2 M HNO_3 (Solution A) and 0.001 mol NH_4VO_3 in 8 mL of 2 M NaOH (Solution B) were prepared. Solution B was slowly brought to Solution A with stirring for 1 hour, and the pH was set to 4 with HCl. After stirring in the dark, yellow precipitates formed, were centrifuged, washed with aqua DM and ethanol, dried at 70°C for 4 hours, and calcined at 400°C for 2 hours, yielding pure $BiVO_4$ powder.

2.2.2 Synthesis of g-C_3N_4

The synthesis of g-C_3N_4 was modified from research Zhao et al. (2021) that began with the calcination process of 5 g of melamine in a sealed alumina container and then heated. After reaching a temperature of 550°C, the sample was left for 4 hours. After natural cooling to ambient temperature, the faint yellowish g-C_3N_4 solids were ground into a powder.

2.2.3 Synthesis of Graphene Quantum Dots (GQDs)

GQDs were synthesized by a simple top-down hydrothermal method modified from Liu et al. (2021). One gram of graphite was included to 80 mL of 65% HNO_3 and magnetically stirred for 12 hours at 80°C. The resulting product was diluted in 200 mL of water, centrifuged, and then brought to 0.0125 M NaOH using a sonicator to set the pH to 11. The mixture was then brought to a Teflon lined autoclave to be heated at 180°C for 12 hours. Afterward, GQDs were passed through a 0.22 μm membrane and the solution was dialyzed using a 1000 Da molecular weight dialysis bag.

Table 1. Volume Variations of The Synthesized GQDs

Material	g-C_3N_4 (C)	$BiVO_4$ (B)	GQDs (G)	Composite
Variations Concentrations	0.001 mol	0.0006 mol	0 mL	CBG-0
	0.001 mol	0.0006 mol	1 mL	CBG-1
	0.001 mol	0.0006 mol	10 mL	CBG-10
	0.001 mol	0.0006 mol	20 mL	CBG-20
	0.001 mol	0.0006 mol	30 mL	CBG-30

2.2.4 Synthesis of g-C_3N_4/$BiVO_4$/GQDs

The results of the synthesis of $BiVO_4$, g-C_3N_4, and GQDs were added in certain proportions (as shown in Table 1). Synthesis begins with g-C3N4 added to 10 mL of methanol and further sonicated for 1 hour for exfoliation. After that, the $BiVO_4$ and GQDs were fed into the g-C_3N_4 suspension which was magnetically stirred until the evaporation of the solvent was completed. The suspension obtained was dried at a temperature of 80°C for 12 hours and calcined in a furnace at a temperature of 400°C for 4 hours then ternary composite was obtained. A similar method was performed for the manufacture of g-C_3N_4/$BiVO_4$ binary composite controls. This method is a modified result of research Yu et al. (2022).

2.2.5 Photocatalysis Studies

The determination of the volume of GQDs at the photocatalyst, pH, and optimal reaction time for MB degradation began with the addition of 0.1 g of g-C_3N_4/$BiVO_4$/GQDs with variations in Table 1 into a beaker glass containing 50 mL of 10 ppm MB solution. The solution was tested under visible light exposure using a blue LED light, with the lamp positioned 20 cm from

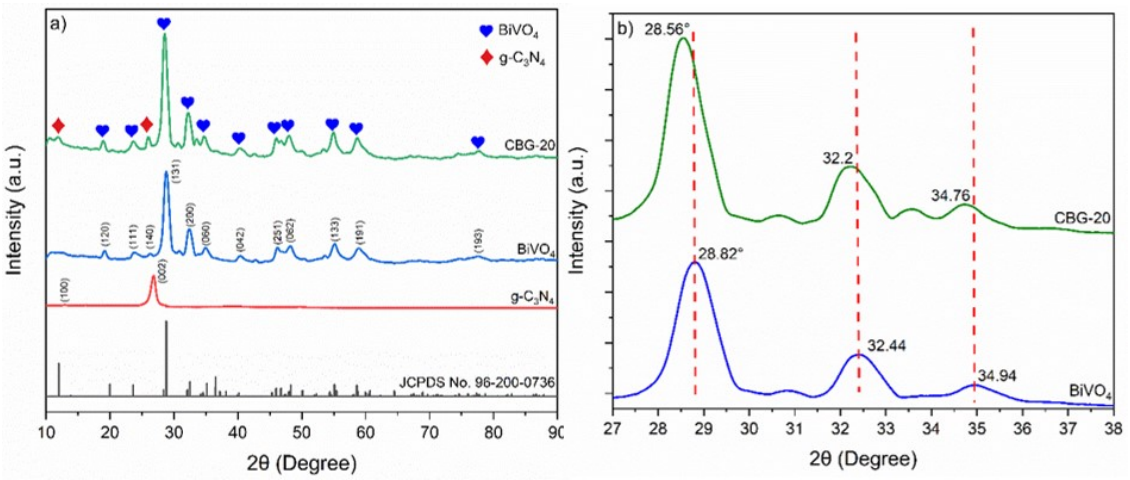

Figure 1. XRD Patterns of $BiVO_4$, g−C_3N_4, and CBG-20 (a); Peak Diffraction in The Range Between 27° to 38° (b)

the solution. Before irradiation, the test was carried out under dark conditions and ambient temperature, the solution is stirred for 30 minutes to form an adsorption-desorption equilibrium before exposure to visible light.

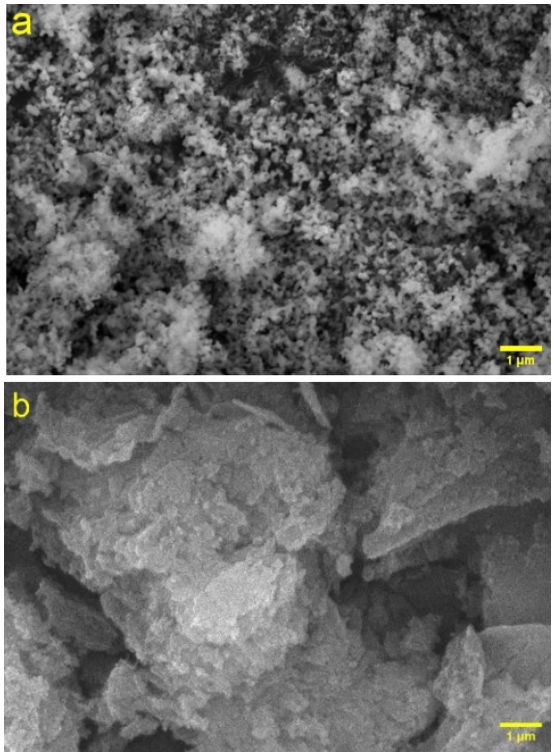

Figure 2. SEM Results of $BiVO_4$ (a) and g-C_3N_4 (b)

After the initiation of the photocatalytic reaction, 5 mL of suspension was taken every 30 minutes for a total reaction time of 210 minutes. Once the most effective photocatalyst ratio was identified, experiments at pH 3, 5, 7, 9, and 11 were conducted. To determine the MB degradation mechanism, benzoquinone ($\cdot O_2^-$ trap), isopropyl alcohol (·OH trap), and ammonium oxalate (hole trap) were added separately under optimal conditions. The species with the lowest degradation % indicated the most significant contributor to photocatalysis.

2.2.6 Determination of Point of Zero Charge (PZC) of g-C_3N_4/$BiVO_4$/GQDs Materials

The PZC composite g-C_3N_4/$BiVO_4$/GQDs was ascertained by the pH drift method. A 0.1 M $NaNO_3$ solution served as the background electrolyte. 0.1 g of the composite (with optimal GQDs volume) was added to 50 mL of $NaNO_3$, set to pH 2-10 with 0.1 M HNO_3 and NaOH. The mixture was shaken for 24 hours at ambient temperature, and the concluding pH was plotted against the initial pH. The PZC was identified where the curve intersected the initial pH line. This method is based on Kalaycıoğlu et al. (2023).

2.2.7 Characterization

The phase crystallinity of the samples was analyzed by an X-ray diffractometer (Shimadzu XRD-7000, Shimadzu, Japan). SEM and TEM analyses were performed with a JEOL JSM-6510LA (JEOL Co. Ltd. Japan) and Hitachi HT 7700 (Hitachi), respectively. The Energy Dispersive X-Ray Spectroscopy (EDX) was carried out for the material surface analysis. A UV–Vis spectrophotometer (UV-1800, Shimadzu, Japan). UV-Vis DRS (Hitachi U-3010, Hitachi, Japan) used to measure the band gap energy of materials. The BET specific surface area was analyzed using Quantachrome Nova 1200e surface analyzer.

3. RESULTS AND DISCUSSION

3.1 XRD Analysis

The diffractograms of $BiVO_4$, g-C_3N_4, and CBG-20 are represented by Figure 1a. The synthesized $BiVO_4$ matches the orthorhombic phase (a = 5.567 Å, b = 15.459 Å, and c = 5.518 Å) possessed by JCPDS No. 96-200-0736. The significant

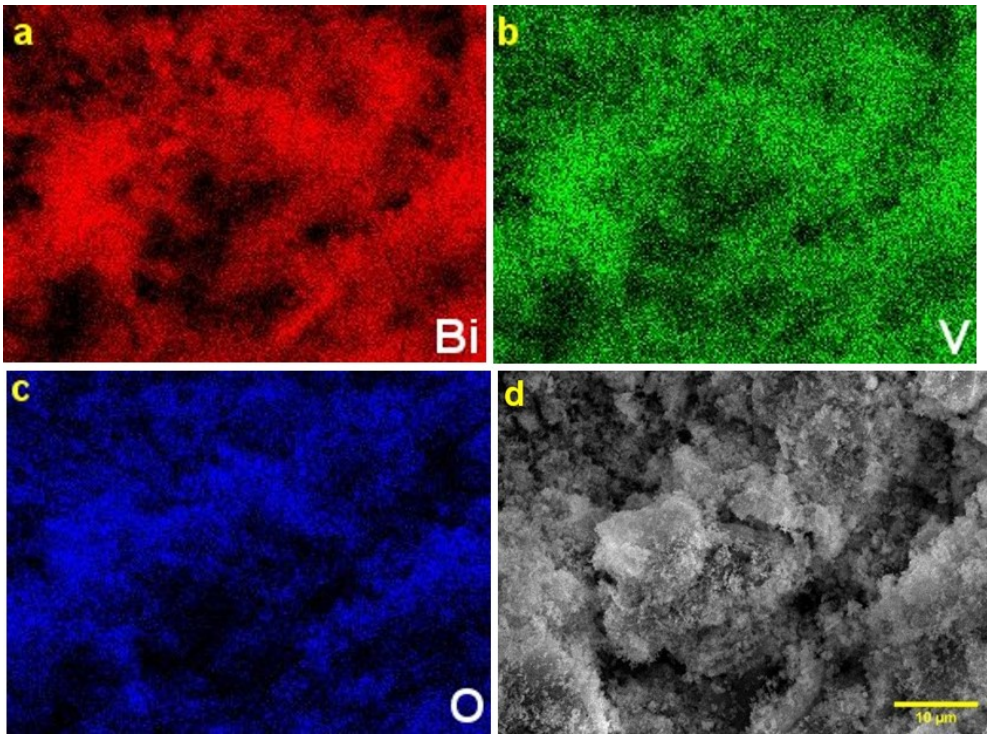

Figure 3. Mapping of CBG-20 Elements (a-c); SEM Image of CBG-20 (d)

diffraction peaks are located at 19.16°, 23.84°, 26.32°, 28.8°, 32.4°, 34.96°, 40.38°, 46.16°, 48.2°, 55.14°, 58.92°, and 77.72° which correspond to the crystal phases (120), (111), (140), (131), (200), (060), (042), (251), (062), (133), (191), and (193), respectively. Meanwhile, the hexagonal phase is owned by g-C3N4 with lattice parameters (a = b = 10.2160 Åand c = 5.9710 Å). The g-C_3N_4 XRD pattern shows an intensive peak at 26.84° possessed by the crystal plane (002) and a weak peak at 12.96° (100) resulting from the interlayer structural packing unit and structural rearrangement within the tri-s-triazine unit plane of the graphite system (Bankole et al., 2021).

Based on the results of XRD analysis, the average crystallite size of the synthesized material can be determined using the Debye-Scherrer equation. The g-C_3N_4, $BiVO_4$, and CBG-20 samples had average crystallite sizes of 2.76 ± 0.816; 7.4 ± 0.1414; and 6.62 ± 0.214, respectively. The CBG-20 composite has 2 peaks that are identical to the peaks of g-C_3N_4, which are at 11.9° and 26.02°. There was a shift in the peak of diffraction in the crystal planes (131), (200), and (060) of $BiVO_4$ after the formation of the CBG-20 ternary composite as evidenced in Figure 1b. All three shifts lead to lower angles caused by the bonding of metal ions on $BiVO_4$ with g-C_3N_4 and GQDs resulting in an increase in lattice spacing. BiVO4 adjusts the layer spacing on g-C_3N_4, indicating the close contact between $BiVO_4$, g-C_3N_4, and GQDs. In addition, GQDs change the loading mode of $BiVO_4$ on g-C_3N_4 because GQDs are anchored on $BiVO_4$ attached to g-C_3N_4 in the Direct Dual Z-scheme. Meanwhile, the peak of diffraction of GQDs cannot be observed due to the small amount of GQDs and its amorphous nature (Feng et al., 2020). The occurence of g-C_3N_4 and GQDs does not alter the orthorhombic structure of $BiVO_4$.

Table 2. EDX Analysis on g-C_3N_4

Elements	Weight (%)	Atomic (%)
C	40.24	44.61
N	54.59	51.90
O	3.87	3.22
Cu	0.87	0.18
Zn	0.44	0.09

3.2 SEM and TEM Analysis

Figure 2a shows $BiVO_4$ has the shape of nanospheres particles with smooth, uniform, and well-crystallized surfaces. As reported by Kamble et al. (2023) the BiVO4 nanoparticles, they change from olive-like structures at lower pH levels to nanospheres when the pH increases from 2.05 to 4.02. The average size of $BiVO_4$ particles through SEM measurement results was 127.4 nm. The g-C_3N_4 sample obtained consists of a layered structure with varying sheet thicknesses shown in Figure 2b. The sheets in the form of nanosheets can be the place where $BiVO_4$ is attached to the composites being synthesized. The lateral size of the synthesized g-C_3N_4 is 2-6 μm. Yu et al. (2022) stated that g-C_3N_4 nanosheets have a typical flexible 2D structure with a lateral size of 6-8 μm. Fig-

ure 3d shows that the $BiVO_4$ particles are well and uniformly distributed on the surface of the g-C_3N_4. The close interface contact between $BiVO_4$ and g-C_3N_4 can accelerate the transfer of photo-excitation carriers. GQDs cannot be identified by SEM.

Table 3. EDX Analysis on CBG-20

Elements	Weight (%)	Atomic (%)
C	20.99	42.50
N	19.42	33.73
O	9.95	15.13
Na	0.61	0.65
Al	0.18	0.17
V	4.15	1.98
Cu	2.18	0.84
Sb	0.72	0.14
Bi	41.79	4.86

EDX analysis was for the g-C_3N_4 material with the results represented in Table 2. C and N content dominate in the composition of g-C_3N_4. Element N is the most dominant compared to C with percentages of 54.59% and 40.24% respectively. The presence of O is caused by the adsorption of oxygen from the air in the precursor during the synthesis of g-C_3N_4 (Bankole et al., 2021).

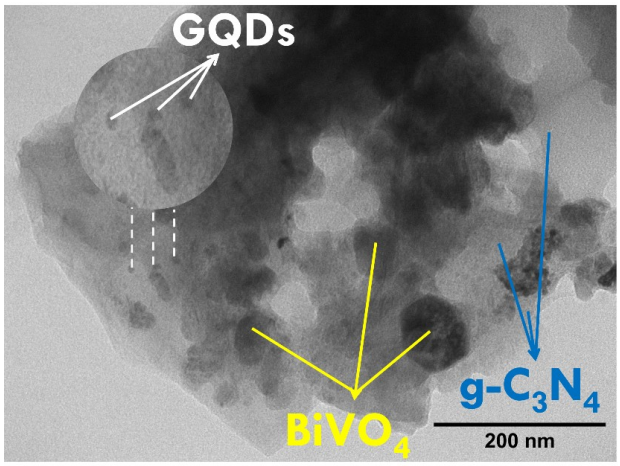

Figure 4. Picture of TEM CBG-20

The composition of the elements was investigated by performing EDX analysis of the prepared ternary composites. Mapping of Bi, V, and O elements is homogeneously dispersed on the CBG-20 ternary composite as evidenced by Figure 3a-d. Table 3 validates the presence of C and N in CBG-20. The percentage of element weight in ternary composites is C by 20.99%, N by 19.42%, Bi by 41.79%, V by 4.15%, and O by 9.95%. This is in line with research Nagar and Basu (2021) that reports that Bi and C elements dominate in the synthesized g-C_3N_4/Ag/$BiVO_4$

$BiVO_4$ particles showing insertion into the structure of g-C_3N_4 and the close interface contact between $BiVO_4$ and g-C_3N_4 with the morphology of nanosheets is evidenced in Figure 4. After the ternary composite is formed, a few GQDs particles cover the surface of the attached $BiVO_4$ as. Based on measurements through TEM analysis, GQDs have an average particle size of 7.4 nm. Liu et al. (2021) revealed that the particle size of GQDs is 6-10 nm. The formation of this interesting morphological structure by the CBG-20 ternary composite can facilitate the photoresponse performance of $BiVO_4$ and facilitate the movement and migration of electron-hole pairs (Fakhrul et al., 2020).

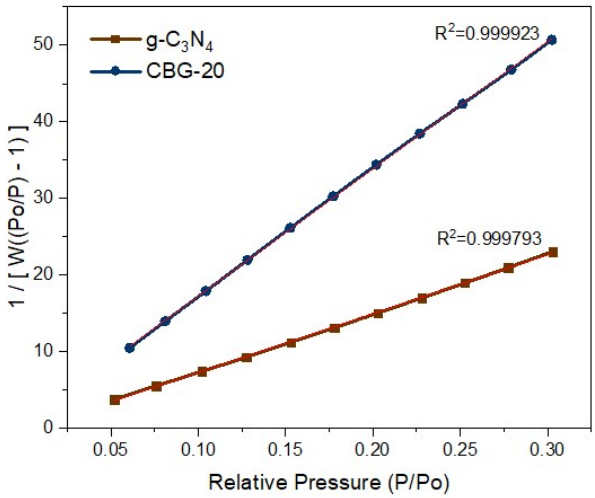

Figure 5. Linear Fit BET Plot of Surface Area for g-C_3N_4 and CBG-20

3.3 BET Surface Area Analysis

The specific surface area of g-C_3N_4 and CBG-20 ternary composites was analyzed by the multipoint Brunauer-Emmett-Teller (BET) method. The surface area plots of g-C_3N_4 and CBG-20 samples shown in Figure 5 show typical linear characteristics with a correlation coefficient of $r \leq 0.999$. The surface area of CBG-20 composite (20.883 m^2/g) is higher than that of $BiVO_4$ (0.3051 m^2/g) reported by Sharifi et al. (2021), but lower than that of g-C_3N_4 (45.614 m^2/g). The high surface area of CBG-20 ternary composites compared to $BiVO_4$ is due to the contribution of g-C_3N_4 which has a broad surface area related to the nanosheet structure of the material. CBG-20 have a lower surface area than g-C_3N_4 because when $BiVO_4$ is composited with g-C_3N_4 and GQDs in the calcination process, the interaction between these materials can result in denser particle aggregations and structures that reduce the overall surface area (Ramírez et al., 2021). This is in line with the study Nagar and Basu (2021) that reported that the surface area of g-C_3N_4 of 87.6 m^2/g is higher than the surface area of 47.5 m^2/g owned by the g-C_3N_4/Ag/$BiVO_4$ ternary composite.

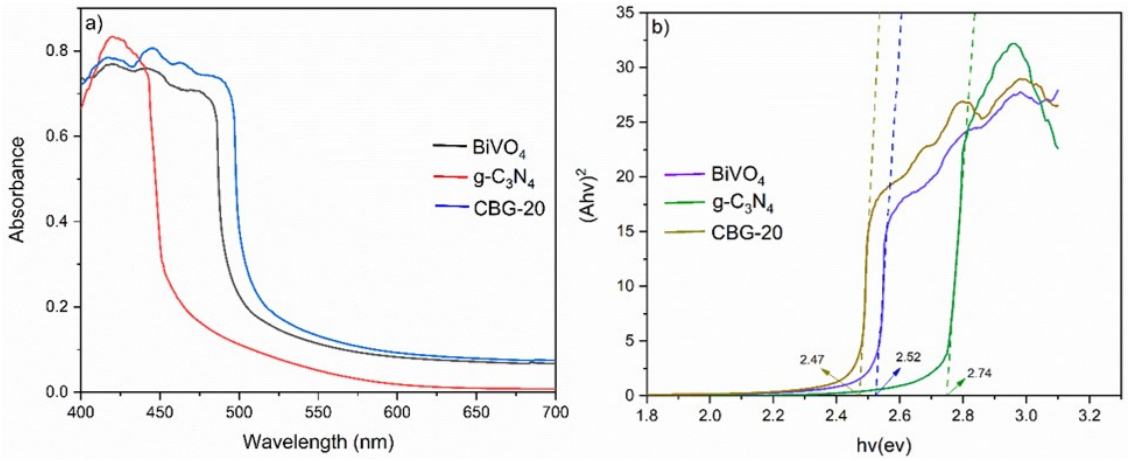

Figure 6. Absorbance Spectra of $BiVO_4$, g-C_3N_4, and CBG-20 (a); Band Gap Energies of g-C_3N_4, $BiVO_4$, and CBG-20 (b)

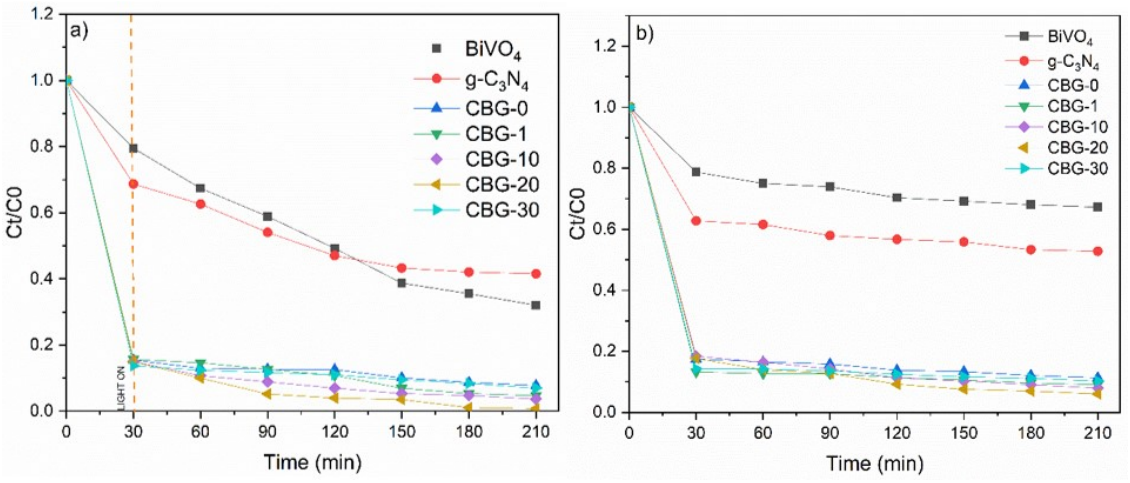

Figure 7. Graph of The Effect of Volume Variation of GQDs on g-C_3N_4/$BiVO_4$/GQDs Composites on MB Photodegradation (Blue Light) (a) and Adsorption in The Dark (b)

3.4 Optical Properties

The absorption threshold of g-C_3N_4 as shown in Figure 6a appears at 460 nm, which is in accordance with previous report by Wu et al. (2021). $BiVO_4$ has an absorption threshold of about 497 nm which falls within the apparent light absorption range, as reported by Li et al. (2021) the orthorhombic $BiVO_4$ absorption threshold (o-$BiVO_4$) value. The CBG-20 ternary composite undergoes redshift with an absorption threshold of 508 nm indicating that the visible light absorption range of $BiVO_4$ and g-C_3N_4 is improved after being composited with GQDs. This proves that CBG-20 can be maximally excited to produce more e^- - h^+ photo-excitation (Ma et al., 2021).

Figure 6b shows that the Eg values of g-C_3N_4, $BiVO_4$, and CBG-20 are 2.74 eV, 2.52 eV, and 2.47 eV, respectively. A report by Chaudhuri et al. (2018) revealed that o-$BiVO_4$ has an Eg of 2.55 eV. The value of Eg g-C_3N_4 has been confirmed based on a study Yu et al. (2022) that reported Eg g-C3N4 of 2.73 eV. Ibarbia et al. (2020) reported that the Eg GQDs value was 2.63 eV. The formation of CBG-20 can decrease the bandgap energy because the doping of GQDs on the strongly bonded $BiVO_4$ to the g-C_3N_4 sheet produces a new energy level of intermediate nature above the valence band formed due to impurities resulting in a reduced bandgap energy (Tahir et al., 2020). The synergistic effect of doping GQDs on CBG-20 also suppress charge recombination with formation of oxygen vacancy to further optimize the charge transfer.

The calculation of the potential values of the conduction band (CB) and valence band (VB) in g-C_3N_4 and $BiVO_4$ can be calculated using Equations 1 and 2 as follows (Bankole et al., 2021):

$$E_{CB} = X - E^e - 0.5E_g \quad (1)$$

$$E_{VB} = E_{CB} + E_g \quad (2)$$

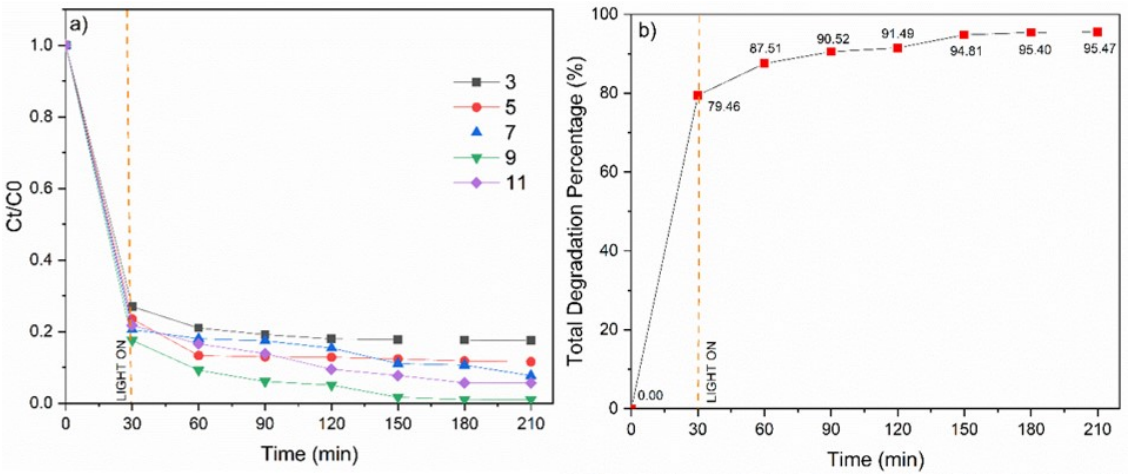

Figure 8. Graph of The Effect of MB pH on MB Photodegradation Using CBG-20 (a) and CBG-20 Total Degradation Against MB (b)

Table 4. Reported Studies on MB Removal Using Photocatalytic Heterojunction Materials

Photocatalysts	Light source	Time (min)	Removal percentage (%)	References
CoO/ZnO	UV	180	67.5	(Rini et al., 2023)
ZnO/Bentonite	UV	180	~71	(Zulkarnain et al., 2024)
$BiVO_4/NiFe_2O_4$	Sunlight	180	80	(Remlalfaka et al., 2021)
Ag/ZnO/GO	Visible	180	85	(Thi et al., 2019)
TiO_2/Fe_3O_4/GO	Visible	90	76	(Nadimi et al., 2019)
ZIF-8/N-CQDs/ZIF-67	Visible	180	94	(Elmorsy et al., 2023)
$WO_3/BiVO_4$/Graphene	Visible	120	63	(Liaqat et al., 2024)
g-C_3N_4/WO_3/rGO	Visible	180	76	(Waheed et al., 2023)
g-C_3N_4/CdS/$BiVO_4$	Visible	120	94.5	(Ranjith et al., 2023)
g-$C_3N_4/BiVO_4$/GQDs	Visible	150	94	This work

where E_{CB}, E_{VB}, E_g, E^e, and X are CB potential, VB potential, band gap, free electron energy at the hydrogen scale, and electronegativity of the semiconductor, respectively. The X values of g-C_3N_4 and $BiVO_4$ are 4.67 eV and 6.16 eV, respectively. The calculated CB and VB potentials of $BiVO_4$ are -1.20 eV and 1.54 eV, respectively, while those of $BiVO_4$ are 0.4 eV and 2.92 eV, respectively. The potential values of CB and VB in g-C_3N_4 and $BiVO_4$ are applied to the analysis of the working mechanism of g-$C_3N_4/BiVO_4$/GQDs in methylene blue photodegradation.

3.5 PZC Analysis

The PZC value obtained is 6.1. When the pH of the methylene blue solution is lower than PZC, the surface of CBG-20 will be positively charged, in opposite, it will be negatively charged when the pH of the methylene blue solution is more than PZC (Jabbar et al., 2023). MB is a cationic dye so that a strong electrostatic attraction occurs between MB molecules and negatively charged CBG-20 in an alkaline environment. Therefore, the best photocatalytic activity occurs in MB solutions that have an alkaline pH, i.e. pH 9. This is shown in Figure 8a.

3.6 Photocatalytic Activity

3.6.1 Optimum Volume for GQDs on g-$C_3N_4/BiVO_4$/-GQDs

Figure 7a presents the relationship between dimensionless concentration changes and the degradation time of $BiVO_4$, g-C_3N_4, CBG-0, CBG-1, CBG-10, CBG-20, and CBG-30 samples. After 210 minutes of visible light exposure, g-C_3N_4 showed the lowest degradation efficiency of 56.33%, and the MB removal percent by BiVO4, CBG-0, CBG-1, CBG-10, CBG-20, and CBG-30 reached 65.49%, 88.86%, 91.95%, 92.83%, 95.65%, and 89.66%, respectively. The CBG-0 binary heterojunction composite has a higher degradation percent than $BiVO_4$ and g-C_3N_4, while the ternary heterojunction photocatalyst CBG-20 has the highest degradation percent. The highest degradation indicates that the loading of GQDs significantly enhances the photocatalytic activity of CBG-0 binary composites. CBG-20

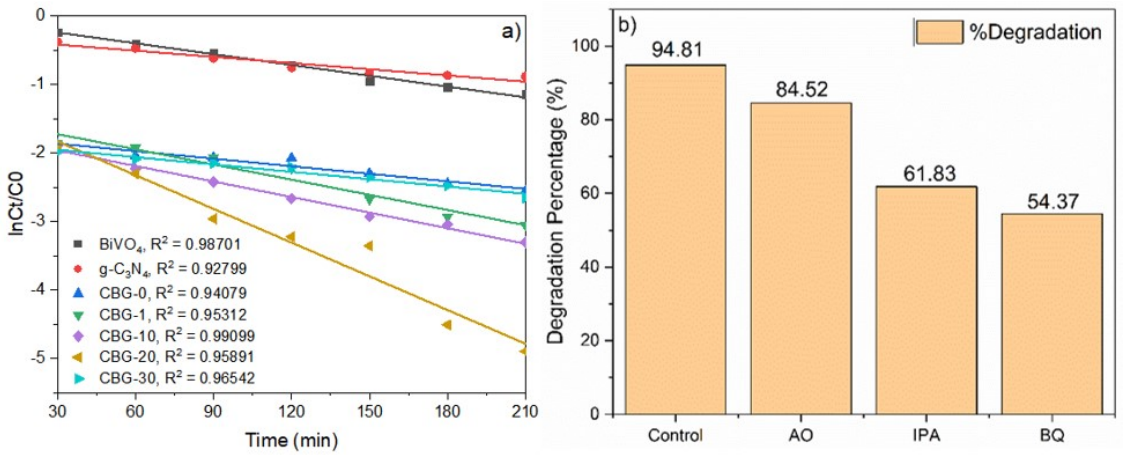

Figure 9. Kinetics Profiles of All Samples on PFO (a) and Effect of Scavengers in The Photocatalytic Degradation Process by CBG-20 in Optimal Condition of MB Solution (b)

structure provides more redox activity at the surfaces compared to binary heterojunction systems and extends the spectral absorption range in the presence of GQDs (Zhao et al., 2021). This result shows that the optimal loading of GQDs is 20 mL results in smooth interface contacts for efficient charge transfer (Kumar et al., 2018). The order of degradation results from the best is as follows: CBG-20 > CBG-10 > CBG-1 > CBG-30 > CBG-0 > BiVO4 > g-C3N4.

The effect of GQDs amount on the photocatalytic activity of ternary composites reveals that with the increase in GQDs content in ternary composites, the MB degradation activity increase. However, this is not the case with CBG-30 because excessive GQDs on the surface of $BiVO_4$ and g-C_3N_4 can reduce the absorption power limiting its photocatalytic performance (Hatefi et al., 2020).

The high adsorption activity (first 30 minutes in dark) in the CBG-0 binary composite shown in Figure 7a. The high adsorption activity reaches 81.49%, owned by the CBG-0 binary composite. This is because of g-C_3N_4 exfoliation triggered by the sonication process during composite synthesis which can peel g-C_3N_4 nanosheets into individual g-C_3N_4 with $BiVO_4$ can be well distributed on the surface of the nanosheets increasing the surface area and providing more active sites for adsorption (Jin et al., 2020). The CBG-1 ternary composite has the highest adsorption activity, reaching 84.29%. This result shows that the result of MB degradation in this study is a synergistic effect of the photocatalytic degradation and adsorption process. Figure 7b confirms that the high adsorption power is possessed by binary and ternary composites. CBG-20 ternary composite has the highest adsorption percentage of 90.60%. However, adsorption for 210 minutes on CBG-20 was not as high as the adsorption-photocatalysis synergy result which reached 95.65%. Based on these two interesting things, it can be concluded that the presence of GQDs does not play a function in increasing the adsorption power of CBG-20 ternary composites but acts in increasing the photocatalytic ability of CBG-20 because it forms a heterostructure that creates photogeneration carriers with strong redox capabilities (Zhong et al., 2023).

3.6.2 Optimum pH for MB Degradation

Figure 8a shows the optimum pH degradation that occurs in an MB solution with a pH of 9. This is in line with the PZC CBG-20 value obtained in this study, which is 6.1. A strong electrostatic pull will occur between the positively charged MB molecule and the negatively charged CBG-20 in an alkaline environment (pH 9 and 11). Meanwhile, the lowest photodegradation performance was detected under acidic conditions (pH 3) due to electrostatic repulsion between MB and CBG-20 molecules. The formation rate of ·OH in the alkaline conditions of pH 9 and 11 is high because there are abundant OH^- ions which cause the formation of ·OH radicals from the oxidation reaction by h^+ with OH^- which makes it easier for CBG-20 to degrade the MB molecule (Shubha et al., 2021).

The performance of CBG-20 in degrading MB dye at pH parameters can also be explained based on the pKa value. MB has a pKa of 3.8 so at pH values higher than 3.8, the dominant methylene blue species in solution is cationic (Sen, 2023). This result supports obtained the PZC CBG-20 value, which is 6.1. If the pH of MB solution is higher than the pKa MB and PZC values of CBG-20, then when the pH of the methylene blue solution is more than PZC, the surface of CBG-20 will be negatively charged and cationic will dominate the methylene blue solution that supports the adsorption of MB.

3.6.3 Identification of Degradation Time

Based on the results of the analysis, Figure 8b shows that the longer the irradiation time, the more the percentage of MB degradation increases with the optimal degradation activity time at 150 min. The optimal time was chosen because after reaching 180 min, the degradation process did not increase significantly and tended to be stable. This happens because

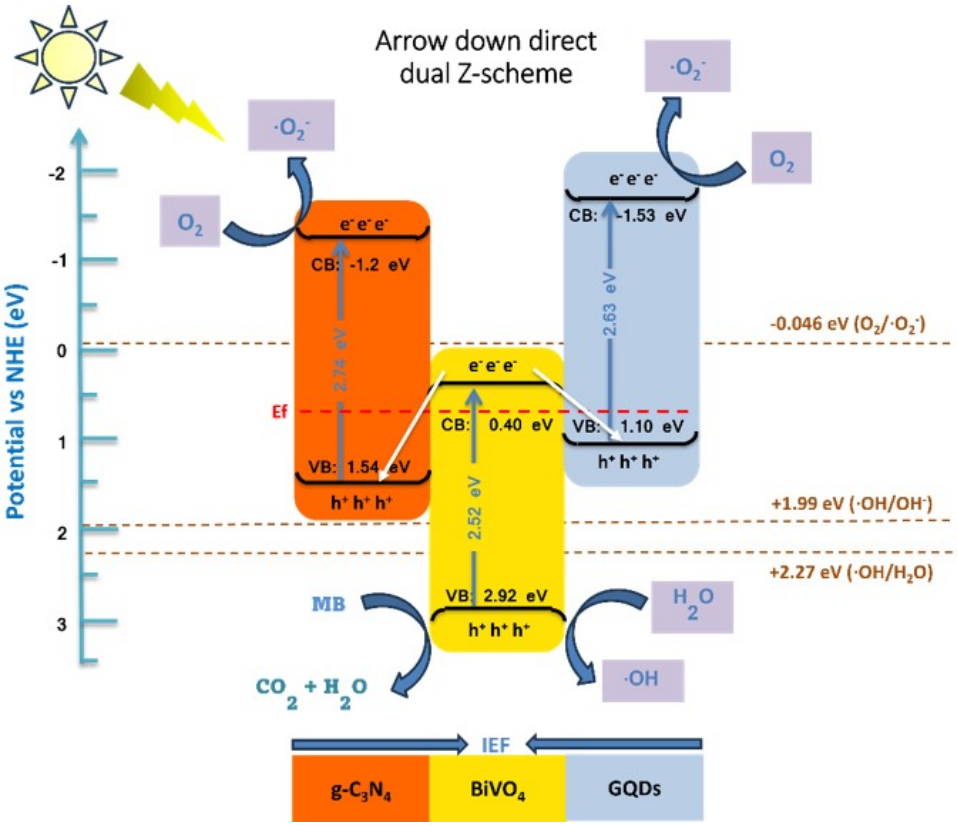

Figure 10. Direct Dual Z-scheme Mechanism on Methylene Blue Photodegradation

the concentration of MB remaining is getting smaller so that the chance of MB molecules interacting with active radicals, such as ·OH or $\cdot O_2^-$ also decreases, which is exacerbated by the increasing number of intermediates that form over time. Intermediates can compete with MB to react with active radicals, thus slowing the rate of MB degradation (Akbari et al., 2020). Based on these results, the selected $BiVO_4$-based ternary composites were compared among various reported investigations on MB degradation which are summarized in Table 4. The enhancement of g-C_3N_4/$BiVO_4$/GQDs ternary nanocomposite for MB decolorization compared to binary composites can be explained by the improved separation and transfer of the charge carriers.

3.6.4 Photocatalytic Degradation Kinetic Rates of g-C_3N_4/-$BiVO_4$/GQDs

The photocatalytic degradation kinetics of all samples can be implemented by the pseudo first order (PFO) reaction equation ln(Ct/Co) = -kt. Figure 9a shows the kinetic data confirmed that the photodegradation of MB follows the pseudo-first-order (PFO) Langmuir–Hinshelwood model. The plot of ln(Ct/Co) vs irradiation time yields a linear relationship showing excellent simulation (R^2>0.9) on PFO. This model is used to explain the reaction kinetics of heterogeneous catalytic reactions, involving solid photocatalysts present in aqueous solution where the reaction takes place on the surface of the solid catalyst (Bahrudin, 2022).

The degradation efficiency and rate constant values demonstrate that the ternary CBG-20 composite exhibits significantly superior photocatalytic activity compared to other photocatalysts. The rate constant values of CBG-20 are 4.3; 5.57; 1.92; 1.61; 1.48; and 1.84 times higher than those of $BiVO_4$, g-C_3N_4, CBG-0, CBG-1, CBG-10, and CBG-30, respectively. This indicates that the the ternary CBG-20 composite is significantly improved result compared to the single photocatalyst and the binary composite.

3.6.5 Photocatalytic Degradation Mechanism

The degradation efficiency of the CBG-20 photocatalyst is inhibited after the addition of AO, BQ, and IPA as scavengers shown by Figure 9b. The scavengers that most inhibit MB degradation are BQ by decreasing degradation activity by -40.44% which indicates that the $\cdot O_2^-$ radical is the dominant active radical species in photocatalytic degradation reactions. This happens because the added scavengers can capture the $\cdot O_2^-$ species produced by the photocatalyst so that the number of $\cdot O_2^-$ that play a role in degrading MB molecules is decreasing. In addition, ·OH and h^+ also play an equally important role in the MB fading reaction. After adding AO and IPA, the degradation efficiency of MB was reduced to 10.29% and 32.98% respectively. The capture of h^+ can inhibit the formation of ·OH, the degradation efficiency of the addition of AO

is slightly higher than that of the addition of IPA which shows h^+ directly oxidizes a small amount of MB (Wang et al., 2022). This implies that the decomposition of MB is the result of the synergistic action of several reactive species with $\cdot O_2^-$ as the dominant reactive species followed by ·OH.

The mechanisms of electron and hole charge transfer have been proposed to follow the direct dual Z-scheme mechanism in Figure 10. Migration of photogeneration carriers can result in e^- being trapped in CB g-C_3N_4 and GQDs and then h^+ being trapped in VB $BiVO_4$. Therefore, the photogenerated e^- in CB g-C_3N_4 (-1.20 eV) and GQDs (-1.6 eV) can reduce O_2 to $\cdot O_2^-$ and photogenerated h^+ species in VB $BiVO_4$ (2.92 eV) can react with H_2O and OH^- molecules to form ·OH. The concentration of $\cdot O_2^-$ produced is higher than that of ·OH because $\cdot O_2^-$ is produced by CB g-C_3N_4 and GQDs, whereas ·OH is produced only by VB $BiVO_4$. The results and analysis correspond with the results of the radical trapping experiment, namely BQ as the most dominant $\cdot O_2^-$ catcher. Therefore, it can be determined that the photocatalytic reaction in the g-C_3N_4/$BiVO_4$/GQDs ternary photocatalyst follows the direct dual Z-scheme transfer mechanism which can improve the efficiency of separation and transfer of the generated photogenerated charge carrier while maintaining redox capabilities for highly efficient MB degradation.

4. CONCLUSIONS

The g-C_3N_4/$BiVO_4$/GQDs ternary composites were successfully synthesized. The synthesis involved calcination of melamine to create hexagonal g-C_3N_4 phase, the coprecipitation method for orthorhombic $BiVO_4$ phase, and the hydrothermal method for GQDs. The narrow band gap (2.47 eV) in the CBG-20 composite compared to the individual components showed increased light absorption and photocatalytic efficiency. The ternary composite CBG-20 showed outstanding photocatalytic activity and structural stability compared to $BiVO_4$ and g-C_3N_4. The optimal condition for degradation is pH 9 for 150 minutes. The results of the scavenger test confirmed that $\cdot O_2^-$ species play the most important photocatalytic role. The process photocatalytic operates via a direct dual g-C_3N_4/$BiVO_4$/GQDs mechanism, offering the benefits of enhanced catalytic activity and excellent stability. As a result, it holds great promise for applications in water pollutant treatment.

5. ACKNOWLEDGEMENT

The authors gratefully acknowledge the financial support provided by the Institute for Research and Community Service of Jenderal Soedirman University through the Riset Dasar Unsoed Scheme with grant No. 26.363/UN23.23.5/PT.01/II/2024.

REFERENCES

Akbari, A., Z. Sabouri, H. A. Hosseini, A. Hashemzadeh, M. Khatami, and M. Darroudi (2020). Effect of Nickel Oxide Nanoparticles as a Photocatalyst in Dyes Degradation and Evaluation of Effective Parameters in Their Removal from Aqueous Environments. *Inorganic Chemistry Communications*, **115**; 107867

Bahrudin, N. N. (2022). Evaluation of Degradation Kinetic and Photostability of Immobilized TiO_2/Activated Carbon Bilayer Photocatalyst for Phenol Removal. *Applied Surface Science Advances*, **7**; 100208

Bankole, O. M., T. D. Olorunsola, and A. S. Ogunlaja (2021). Photocatalytic Decontamination of Toxic Hexavalent Chromium in Water Over Graphitic Carbon Nitride Supported Sulfur Nanoparticles. *Journal of Photochemistry and Photobiology A: Chemistry*, **405**; 112934

Chaudhuri, A., L. Mandal, X. Chi, M. Yang, M. C. Scott, M. Motapothula, X. J. Yu, P. Yang, Y. Shao-Horn, T. Venkatesan, A. T. S. Wee, and A. Rusydi (2018). Direct Observation of Anisotropic Small-hole Polarons in an Orthorhombic Structure of $BiVO_4$ Films. *Physical Review B*, **97**(19); 195150

Cheng, C., Q. Liang, M. Yan, Z. Liu, Q. He, T. Wu, S. Luo, Y. Pan, C. Zhao, and Y. Liu (2022). Advances in Preparation, Mechanism and Applications of Graphene Quantum Dots/Semiconductor Composite Photocatalysts: A Review. *Journal of Hazardous Materials*, **424**; 127721

Dihom, H. R., M. M. Al-Shaibani, R. M. S. Radin Mohamed, A. A. Al-Gheethi, A. Sharma, and M. H. B. Khamidun (2022). Photocatalytic Degradation of Disperse Azo Dyes in Textile Wastewater Using Green Zinc Oxide Nanoparticles Synthesized in Plant Extract: A Critical Review. *Journal of Water Process Engineering*, **47**; 102705

El-Yazeed, W. S. A., S. A. El-Hakam, A. A. Salah, and A. A. Ibrahim (2021). Fabrication and Characterization of Reduced Graphene-$BiVO_4$ Nanocomposites for Enhancing Visible Light Photocatalytic and Antibacterial Activity. *Journal of Photochemistry and Photobiology A: Chemistry*, **417**; 113362

Elmorsy, E. S., W. A. Amer, A. Mahrous, and M. M. Ayad (2023). Insight into the Novel ZIF-8@ N-CQDs/ZIF-67 Nanocomposite for Photocatalytic Degradation of Methylene Blue under Visible Light Irradiation. *Materials Science and Engineering: B*, **298**; 116900

Fakhrul, M., R. Samsudin, A. Dumas, R. Bashiri, N. M. Mohamed, and S. Sufian (2020). Development of the g−C_3N_4/$BiVO_4$ Microflower Photocatalyst for Photocatalytic Degradation of Amoxicillin and Hydrogen Production. *Malaysian Journal of Microscopy*, **16**(1); 180–187

Feng, S., T. Chen, Z. Liu, J. Shi, X. Yue, and Y. Li (2020). Z-Scheme CdS/CQDs/g−C_3N_4 Composites with Visible-Near-Infrared Light Response for Efficient Photocatalytic Organic Pollutant Degradation. *Science of The Total Environment*, **704**; 135404

Hatefi, R., A. Mashinchian-Moradi, H. Younesi, and S. Nojavan (2020). Graphene Quantum Dots Based on Maltose as a High Yield Photocatalyst for Efficient Photodegradation of Imipramine in Wastewater Samples. *Journal of Environmental Health Science and Engineering*, **18**; 1531–1540

Ibarbia, A., H. J. Grande, and V. Ruiz (2020). On the Factors

Behind the Photocatalytic Activity of Graphene Quantum Dots for Organic Dye Degradation. *Particle and Particle Systems Characterization*, **37**(5); 2000061

Jabbar, Z. H., A. A. Okab, B. H. Graimed, M. A. Issa, and S. H. Ammar (2023). Photocatalytic Destruction of Congo Red Dye in Wastewater Using a Novel Ag_2WO_4/Bi_2S_3 Nanocomposite Decorated g$-C_3N_4$ Nanosheet as Ternary S-Scheme Heterojunction: Improving the Charge Transfer Efficiency. *Diamond and Related Materials*, **133**; 109711

Jin, C., W. Li, Y. Chen, R. Li, J. Huo, Q. He, and Y. Wang (2020). Efficient Photocatalytic Degradation and Adsorption of Tetracycline Over Type-II Heterojunctions Consisting of ZnO Nanorods and K-Doped Exfoliated g$-C_3N_4$ Nanosheets. *Industrial and Engineering Chemistry Research*, **59**(7); 2860–2873

Kalaycıoğlu, Z., B. Özuğur Uysal, O. Pekcan, and F. B. Erim (2023). Efficient Photocatalytic Degradation of Methylene Blue Dye from Aqueous Solution with Cerium Oxide Nanoparticles and Graphene Oxide-Doped Polyacrylamide. *ACS Omega*, **8**(14); 13004–13015

Kamble, G. S., T. S. Natarajan, S. S. Patil, M. Thomas, R. K. Chougale, P. D. Sanadi, U. S. Siddharth, and Y. C. Ling (2023). $BiVO_4$ as a Sustainable and Emerging Photocatalyst: Synthesis Methodologies, Engineering Properties, and Its Volatile Organic Compounds Degradation Efficiency. *Nanomaterials*, **13**(9); 1528

Kumar, R., A. Sudhaik, A. A. P. Khan, P. Raizada, A. M. Asiri, S. Mohapatra, S. Thakur, V. K. Thakur, and P. Singh (2022). Current Status on Designing of Dual Z-Scheme Photocatalysts for Energy and Environmental Applications. *Journal of Industrial and Engineering Chemistry*, **106**; 340–355

Kumar, S., A. Dhiman, P. Sudhagar, and V. Krishnan (2018). ZnO-Graphene Quantum Dots Heterojunctions for Natural Sunlight-Driven Photocatalytic Environmental Remediation. *Applied Surface Science*, **447**; 802–815

Li, P., Y. Hu, D. Lu, J. Wu, and Y. Lv (2023). Study on g$-C_3N_4/BiVO_4$ Binary Composite Photocatalytic Materials. *Micromachines*, **14**(3); 639

Li, Y., B. Yang, and B. Liu (2021). Synthesis of $BiVO_4$ Nanoparticles with Tunable Oxygen Vacancy Level: The Phenomena and Mechanism for Their Enhanced Photocatalytic Performance. *Ceramics International*, **47**(7); 9849–9855

Liaqat, M., R. M. Munir, I. Maryam, T. Iqbal, S. Afsheen, A. G. Nabi, R. R. M. Khan, A. El-marghany, I. Warad, and A. Basit (2024). Synthesis and Characterization of $WO_3/BiVO_4$/Graphene Ternary Nanocomposites for the Photodegradation of Methlyene Blue and Tetracycline. *Materials Chemistry and Physics*, **320**; 129465

Liu, Y., X. Zhang, X. Li, and Z. Zhou (2024). Visible Light Driven S-Scheme GQDs/BiOBr Heterojunction with Enhanced Photocatalytic Degradation of Rhodamine B and Mechanism Insight. *Journal of Water Process Engineering*, **57**; 104588

Liu, Z., F. Li, Y. Luo, M. Li, G. Hu, X. Pu, T. Tang, J. Wen, X. Li, and W. Li (2021). Size Effect of Graphene Quantum Dots on Photoluminescence. *Molecules*, **26**(13); 3922

Ma, C., J. Lee, Y. Kim, W. C. Seo, H. Jung, and W. Yang (2021). Rational Design of $\alpha-Fe_2O_3$ Nanocubes Supported $BiVO_4$ Z-Scheme Photocatalyst for Photocatalytic Degradation of Antibiotic Under Visible Light. *Journal of Colloid and Interface Science*, **581**; 514–522

Mansha, M. S., T. Iqbal, M. Farooq, K. N. Riaz, S. Afsheen, M. S. Sultan, N. Al-Zaqri, I. Warad, and A. Masood (2023). Facile Hydrothermal Synthesis of $BiVO_4$ Nanomaterials for Degradation of Industrial Waste. *Heliyon*, **9**(5); e15978

Nadimi, M., A. Ziarati Saravani, M. A. Aroon, and A. Ebrahimian Pirbazari (2019). Photodegradation of Methylene Blue by a Ternary Magnetic TiO_2/Fe_3O_4/Graphene Oxide Nanocomposite Under Visible Light. *Materials Chemistry and Physics*, **225**; 464–474

Nagar, A. and S. Basu (2021). Ternary g$-C_3N_4$/Ag/$BiVO_4$ Nanocomposite: Fabrication and Implementation to Remove Organic Pollutants. *Environmental Technology and Innovation*, **23**; 101646

Ramírez, A. E., M. Montero-Muñoz, L. L. López, J. E. Ramos-Ibarra, J. A. H. Coaquira, B. Heinrichs, and C. A. Páez (2021). Significantly Enhancement of Sunlight Photocatalytic Performance of ZnO by Doping with Transition Metal Oxides. *Scientific Reports*, **11**(1); 2804

Ranjith, R., N. Karmegam, M. Alsawalha, X. Hu, and K. Jothimani (2023). Construction of g$-C_3N_4$/CdS/$BiVO_4$ Ternary Nanocomposite with Enhanced Visible-Light-Driven Photocatalytic Activity Toward Methylene Blue Dye Degradation in the Aqueous Phase. *Journal of Environmental Management*, **330**; 117132

Remlalfaka, W., C. Murugesan, P. N. Anantharamaiah, and N. M. Prabu (2021). Fabrication of Magnetically Recoverable $BiVO_4/NiFe_2O_4$ Composites for the Photocatalytic Degradation of Methylene Blue. *Ceramics International*, **47**(8); 11526–11535

Riapanitra, A., T. Setyaningtyas, and G. H. Haryadinaru (2024). Photodegradation of Methylene Blue Dye Using $BiVO_4$/g$-C_3N_4$ Composites Under Visible Light Irradiation. *Jurnal Kimia Sains Dan Aplikasi*, **27**(8); 363–370

Riapanitra, A., T. Setyaningtyas, K. Riyani, R. Andreas, A. L. Ariyanti, and U. Sulaeman (2022). Synthesis of Vanadium Oxide Material and Its Photocatalytic Activity in the Degradation of Methylene Blue. In *AIP Conference Proceedings*, volume 2553

Rini, N. P., N. I. Istiqomah, Sunarta, and E. Suharyadi (2023). Enhancing Photodegradation of Methylene Blue and Reusability Using CoO/ZnO Composite Nanoparticles. *Case Studies in Chemical and Environmental Engineering*, **7**; 100301

Sarwar, A., A. Razzaq, M. Zafar, I. Idrees, F. Rehman, and W. Y. Kim (2023). Copper Tungstate ($CuWO_4$)/Graphene Quantum Dots (GQDs) Composite Photocatalyst for Enhanced Degradation of Phenol Under Visible Light Irradia-

tion. *Results in Physics*, **45**; 106253
Sen, T. K. (2023). Adsorptive Removal of Dye (Methylene Blue) Organic Pollutant from Water by Pine Tree Leaf Biomass Adsorbent. *Processes*, **11**(7); 1877
Sharifi, T., D. Crmaric, M. Kovacic, M. Popovic, M. K. Rokovic, H. Kusic, D. Jozić, G. Ambrožić, D. Kralj, J. Kontrec, B. Zener, U. L. Stangar, D. D. Dionysiou, and A. L. Bozic (2021). Tailored $BiVO_4$ for Enhanced Visible-Light Photocatalytic Performance. *Journal of Environmental Chemical Engineering*, **9**(5); 106025
Shubha, J. P., H. S. Savitha, S. F. Adil, M. Khan, M. R. Hatshan, K. Kavalli, and B. Shaik (2021). Straightforward Synthesis of Mn_3O_4/ZnO/Eu_2O_3-Based Ternary Heterostructure Nano-Photocatalyst and Its Application for the Photodegradation of Methyl Orange and Methylene Blue Dyes. *Molecules*, **26**(15); 4661
Su, F., P. Li, J. Huang, M. Gu, Z. Liu, and Y. Xu (2021). Photocatalytic Degradation of Organic Dye and Tetracycline by Ternary Ag_2O/AgBr-CeO_2 Photocatalyst Under Visible-Light Irradiation. *Scientific Reports*, **11**(1); 85
Tahir, M., S. Tasleem, and B. Tahir (2020). Recent Development in Band Engineering of Binary Semiconductor Materials for Solar Driven Photocatalytic Hydrogen Production. *International Journal of Hydrogen Energy*, **45**(32); 15985–16038
Thi, V. H. T., T. H. Cao, T. N. Pham, T. T. Pham, and M. C. Le (2019). Synergistic Adsorption and Photocatalytic Activity Under Visible Irradiation Using Ag-ZnO/GO Nanoparticles Derived at Low Temperature. *Journal of Chemistry*, **2019**; 2979517
Waheed, Z., S. Ghazanfar, M. Usman, H. M. Asif, M. Tariq, K. Mahmood, A. Haider, and M. Sirajuddin (2023). Synthesis and Characterization of Ternary Composite g−C_3N_4-WO_3/rGO for Photocatalytic Activity in Degradation of Methylene Blue. *Bulletin of the Chemical Society of Ethiopia*, **37**(5); 1123–1131
Wang, S., L. Zhao, L. Gao, D. Yang, S. Wen, W. Huang, Z. Sun, J. Guo, X. Jiang, and C. Lu (2022). Fabrication of Ternary Dual Z-Scheme AgI/$ZnIn_2S_4$/$BiVO_4$ Heterojunction Photocatalyst with Enhanced Photocatalytic Degradation of Tetracycline Under Visible Light. *Arabian Journal of Chemistry*, **15**(10); 104159
Wu, Y., X. Zhao, S. Huang, Y. Li, X. Zhang, G. Zeng, L. Niu, Y. Ling, and Y. Zhang (2021). Facile Construction of 2D g−C_3N_4 Supported Nanoflower-like $NaBiO_3$ with Direct Z-Scheme Heterojunctions and Insight into Its Photocatalytic Degradation of Tetracycline. *Journal of Hazardous Materials*, **414**; 125547
Yu, F., F. Gong, Q. Yang, and Y. Wang (2022). Fabrication of a Magnetic Retrievable Dual Z-Scheme g−C_3N_4/$BiVO_4$/$CoFe_2O_4$ Composite Photocatalyst with Significantly Enhanced Activity for the Degradation of Rhodamine B and Hydrogen Evolution Under Visible Light. *Diamond and Related Materials*, **125**; 109004
Zhao, G., J. Ding, F. Zhou, X. Chen, L. Wei, Q. Gao, K. Wang, and Q. Zhao (2021). Construction of a Visible-Light-Driven Magnetic Dual Z-Scheme $BiVO_4$/g−C_3N_4/$NiFe_2O_4$ Photocatalyst for Effective Removal of Ofloxacin: Mechanisms and Degradation Pathway. *Chemical Engineering Journal*, **405**; 126704
Zhao, Z., J. Wang, C. Xu, Z. Du, R. Yu, Y. Zhao, J. Han, J. Zuo, Z. Guo, C. Tang, and Y. Fang (2024). Construction of a Novel Ternary GQDs/g−C_3N_4/ZIF-67 Photocatalyst for Enhanced Photocatalytic Carbon Dioxide Reduction. *Catalysts*, **14**(6); 334
Zhong, X., Y. Li, H. Wu, and R. Xie (2023). Recent Progress in $BiVO_4$-Based Heterojunction Nanomaterials for Photocatalytic Applications. *Materials Science and Engineering: B*, **289**
Zulkarnain, Y. M. Hakim, E. Melwita, and R. Mohadi (2024). The Effects of Hydrothermal Temperatures on ZnO-Bentonite Composite Synthesis on Adsorption and Photodegradation of Methylene Blue Dye. *Science and Technology Indonesia*, **9**(4); 1033–1041

